Title: Role of endothelial micronuclei-contained DNA in atherosclerosis

Lucia Natarelli[1†], Zahra Abedi Kichi[1], Elizabeth Josefina Mann Fallenbuchel[1], Luca Parca[2], Tommaso Mazza[2], Christian Weber[1]

[1] Institute for Cardiovascular Prevention (IPEK), Ludwig-Maximilians-Universität (LMU), 800336 Munich, Germany.
[2] IRCCS Casa sollievo della Sofferenza, Laboratory of Bioinformatics, 71013 San Giovanni Rotondo (FG), Italy.
[†]Corresponding author

Abstract

Atherosclerosis is a complex disease, often associated with hyperlipidaemia, that affects vessel trees under altered hemodynamic forces. However, shear stress is not themselves responsible for atherosclerosis genesis. Chromosomal mutations and DNA damage emerged as key epigenetic variations responsible of regional phenotypic heterogeneity, especially in endothelial cells (ECs) lining arterial tree. We previously reported that aortic ECs show a physiological propensity to accumulate damage in micronuclei (MN), usually generated in hyperproliferative cells. Hyperlipidaemia exacerbates DNA damage and MN formation in these ECs, but the interplay between endothelial MN and atherosclerosis is unknown. Here we show that low shear stress promotes physiologic MN in proliferative human ECs, whereas hyperlipidaemia enhanced the formation of pathological MN. DNA signatures were investigated by WGS of MN and main nuclei containing DNA in synthesis or damaged. Duplications in known loci of atherosclerosis susceptibility were in physiological MN. Pathological MN comprise duplications of pro-inflammatory genes, and mutations of cell cycle check and repair genes. Transcriptional relevance was confirmed for all key DNA damage repair markers of homologous recombination. Hyperlipidaemia enhanced the accumulation of MN with defects in Lamin B1, involved in double strand breaks repair by relocating damaged DNA at the nuclear periphery. Taken together, our work indicates a role for DNA signatures relocated in endothelial MN on atherosclerosis, which accumulate upon impaired DNA repair.

Main

The presence of atherosclerotic plaques at arterial trees, even in absence of risk factors (1, 2), raises the question of how these sites are more susceptible to plaque formation compared to linear arterial tracts. The prevalent explanation is that hemodynamic forces influence the physiological state of vessel trees (3), inflicting low-grade injury to ECs that protect arteries from denudation by enhancing their proliferative rate (4). However, recent studies have demonstrated that flow dynamics are not themselves responsible for the genesis of atherosclerosis (3, 5) and that epigenetic variations, like chromosomal aberrations and damage, are associated with plaque development. As all proliferating cells are susceptible to mitotic aberrations (6), we previously demonstrated that ECs at vessel trees are characterized by an increased frequency of extranuclear structures termed micronuclei (MN) and DNA damage (DD) during atherosclerosis (7, 8). MN biological function is unknown, but they show an extremely varied origin (9). In MNated cells, proceeding with the final phase of cell division before the checkpoints for micronuclear DNA defects are completed leads to accumulation of defective DNA or reincorporation into the main nucleus, promoting mitotic catastrophe (6, 10). Despite the molecular mechanisms of MN inheritance remain elusive, genes relocated in MN appear to be expressed more frequently and asynchronously than those expressed by major nuclei (11). Moreover, asynchronisms in damaged DNA seems to be associated with defective relocation of DD at nuclear periphery, a mechanism partly depending on lamin integrity as main structural protein of major and MN (12, 13). Despite the biological function of MN and their interplay with atherosclerosis remain largely unknown, regardless the existence of genome instability, MN can significantly disrupt cellular phenotype.

Physiological MN arise from proliferative ECs

We first confirmed that MN formation observed in murine aortic ECs (MAoECs)(7) occurred in primary human AoECs (HAoECs). We extended our findings to show that static flow and low shear stress (LSS), characterizing arterial trees, but not high shear stress (HSS), predispose ECs to MN formation in proliferating (EdU^+) compared to nonproliferating ECs (**Fig1a,b and Suppl. Fig1a,b**). EC proliferation protects arterial tree from denudation but may also increase the frequency of mitotic errors and MN. Accordingly, proliferation persisted at later time points, as well as the MN frequency in proliferating *vs.* nonproliferating AoECs (**Fig1b and Suppl. Fig1b**). *En face* immunofluorescence (IF) of murine aortae confirmed the proliferative phenotype of $CD31^+$ECs lining arterial bifurcations upon physiological disturbed flow and their predisposition to MN formation compared to thoracic tracts under laminar flow (**Fig1c**). The number of MN did not increase over time, but the number of MN was always higher in proliferating compared to nonproliferating ECs (**Fig1d**).

To establish the cell cycle phase at which MN originated, HAoECs were released from their synchronized interphase and let to proceed till their metaphase using colcemid (**Suppl. Fig1c**). MN formation physiologically occurred only after the release of ECs from their metaphasic block (**Fig1e and Suppl. Fig1c**), leading to nuclear buds' formation during cytokinesis (**Fig1e**). Similar results were observed in unsynchronized cells (**Fig1e**). To explore whether DNA relocated in physiological MN duplicates synchronously and within one cell cycle, we live-track cell cycle of HAoECs expressing Cdt1-*TagRFP* and geminin-*emGFP* indicators (**Suppl. Fig1d**). Confocal live-3D stacks confirmed the cytokinesis as phase at which physiological MN originate, as well as their ability to efficiently duplicate their DNA content synchronously to their principal nucleus (PN) (**Fig1e and Suppl. Fig1d**). Most of post-mitotic MN contained DNA fragments arising from centromeric ($CENP\text{-}B^+$) truncated fragments ($TRAF1^-$) (**Suppl. Fig1e**).

Pathological MN arise from mitotic asynchronisms in ECs

Hyperlipidaemia inhibits proliferation of ECs at arterial trees (7, 14), arguing against a contribution of MN deriving from proliferative ECs on atherosclerosis. However, EC proliferation might be affected by oxidized low density lipoproteins (oxLDL), used as a surrogate for hyperlipidaemia *in vitro*, depending on the magnitude of exposure (12, 13). Indeed, a short exposure to low (25-50μg/ml) but not high doses (100μg/ml) of oxLDL enhanced EC proliferation, whereas prolonged exposure to all oxLDL doses suppressed proliferation of murine (**Suppl. Fig1f**) and human AoECs (**Suppl. Fig1g**), which was not reflected in the onset of apoptosis or oxidative stress (**Suppl. Fig1h**). The steady, concentration-dependent increase in MN occurred initially in proliferating cells (4h), and gradually shifted (24h) to nonproliferating ECs (48h) (**Fig1f and Suppl. Fig1f,g**). The shift became less and less gradual as the dose of oxLDL used increased (**Fig1f**). To translate data *in vivo*, $Apoe^{-/-}$ mice were fed for 4 and 12 weeks with a ND or western diet (WD). EC proliferation at arterial tree was enhanced during atherogenesis (4 weeks) but suppressed during atheroprogression (12 weeks) (**Fig1g**). Concomitantly, a chronic formation of pathological MN was observed at 4 weeks primarily in proliferating ECs, whereas at 12 weeks almost 90% of detected MN enriched nonproliferating ECs (**Fig1g**). These results indicate that hyperlipidaemia promotes a pathological hyperproliferative phenotype in ECs at arterial tree, increasing the frequency of MN. Furthermore, this susceptibility influences primarily proliferating ECs at arterial tree that physiologically contain MN.

To assess the cell cycle phase at which oxLDL-deriving MN originated, synchronized HAoECs were released up to their metaphase as for untreated HAoECs (**Suppl. Fig1c**). Pre-metaphasic fragments were already detected in oxLDL-treated ECs (**Fig1h and Suppl. Fig1i**) and persisted in cells during anaphase and telophase (**Suppl. Fig1i**). Like in unsynchronized cells, oxLDL-treated cells enhanced chromatin bridges characterizing MN of post-mitotic origin (**Fig1h**). Mis-segregation of entire chromosomes (CENP-B$^+$ TRAF1$^+$) and multicentric fragments (poli CENP-B$^+$) was observed in oxLDL deriving MN (**Suppl. Fig1e**). Live track of Cdt1-*TagRFP* and geminin-*emGFP* indicators revealed that pathological MN preserved the ability to duplicate their DNA content (**Suppl. Fig1j**), but asynchronously with their principal nucleus (PN) (**Fig1h**). Asynchronous DNA synthesis was corroborated *in vitro* and in hyperlipidaemic mice by analysing Ki67$^{+/-}$ MN in Ki67$^{+/-}$ PN, which levels reach the maximum in G_1/S and G_2/M phases (15), as asynchronous indicators (**Suppl. Fig1k and Fig1i,j**). Synchronization between MN and PN was altered by hyperlipidaemia and oxLDL, which initially promoted an asynchronized MNeic DNA synthesis in both proliferating and nonproliferating ECs (**Suppl. Fig1k**). Interestingly, although proliferation was inhibited by chronic exposure to oxLDL and hyperlipidaemia, asynchronous MNeic DNA synthesis persisted at 24h and at 12 weeks in nonproliferating ECs (**Suppl. Fig1k and Fig1i,j**). In line with our and previous findings that uncontrolled EC proliferation sustains MN formation and mitotic errors, hyperproliferation might enhance MN formation and promote asynchronous DNA synthesis, generating a source of potentially unrepaired DNA that might support atherosclerosis.

Pathological MN accumulate damaged DNA

We previously reported that prolonged exposure to hyperlipidaemia enhances mitotic errors and DD relocation in MN deriving from ECs at vessel trees (7). We extended our findings in human ECs and investigated the correlation between asynchronous proliferation and DD in MN. Analysis of gamma H2A histone family member X (γH2AX), marker of DD phosphorylated to recruit initiators of DDR, indicated oxLDL- and hyperlipidaemia-driven as sources for DD, initially extruded from hyperproliferative cells (**Fig2a,e**), and accumulated in MN from nonproliferating ECs at chronic stages (**Figb,f**). Multiple comparison corroborated γH2AX$^+$Ki67$^+$ (double positive, DP) ECs as a source of γH2AX$^+$MN at 24h and 4 weeks, when DNA asynchronism was at its maximum (**Fig2c,e**). Prolonged exposure to high levels of lipids sustained the accumulation of MNeic DD in nonproliferating γH2AX$^+$PN (**Fig2d,f**). Taken together, these data confirmed that EC exposure to genotoxic stresses sustain an asynchronous DNA replication that increase the frequency of mitotic errors and DD. Prolonged exposure to hyperlipidaemia may affect DDR, leading to DD accumulation in MN from nonproliferating ECs. Accordingly, inhibition of the MNeic antagonist lncWDR59 (7) in oxLDL-treated ECs did not enhance MN formation, but rather promoted the accumulation of MNeic DD (**Suppl. Fig2a**).

To assess whether oxLDL predispose ECs to MN retention and to corroborate the role of MN signatures in arterial predisposition to atherosclerosis, we developed a novel strategy to isolate fluorescent MN (2-8μm) by size-gated FACS sorter (**Suppl. Fig2b**). Following FACS confirmation of MN identity, compared to PN (15-20 μm)(**Suppl. Fig2c**), DNA synthesis and damage (**Suppl. Fig2d**), and excluding their origin from dead cells or debris (**Suppl. Fig2e**), live cell imaging indicated that ECs required 6h to engulf MN in their cytoplasm (**Fig2g**). ECs activated a physiological response against these pathological but not physiological MN, as indicated by activation of pro-angiogenic p38 (**Fig2g**), and slight activation of Caspase3, inactive in oxLDL recipient ECs (**Fig2b**). In contrast, oxLDL treatment enhanced MN retention, especially of oxLDL-deriving MN, which DNA was reincorporated in the PN (**Fig2g**), indicating

that oxLDL invalidated MN clearance and might promote the expression of asynchronized and damaged DNA enriched in MN. OxLDL-deriving MN, but not oxLDL pre-treatment, activated caspase 3 (~20%) (**Fig2g**). Taken together, these data indicate a role for oxLDL-driven MN signatures in atherosclerosis.

Aortic EC phenotype arise from MNeic DNA signatures, mutated by oxLDL

To dissect selective signatures relocated in MN that might determine EC phenotype and contribute to athero-susceptibility of arterial tree, we isolated DNA from FACS sorted MN and PN to identify functional annotation for human copy number variants (CNVs) and structural variants (SVs) in MNeic genes by whole genome sequencing (WGS) (**Suppl. Fig3a**). Aneuploidy landscapes of CNVs revealed a high mis-segregation error among chromosomes (Chr) 15 (12%) and 19 (26,2%) in MN compared to all other Chr, independently from oxLDL treatment, which enhanced Chr19 mis-segregation of an additional 8,3% (**Fig3a**). These data might sustain the Chr19 locus association with incidences (16). CNVs were identified for 7.355 protein-coding genes (**Suppl. Fig3b,c**), 2.424 out of which contained SV duplications in MN and PN, and encoded for inflammation, oxidative damage, histones modifications, RNA transcription, Chr relaxation, and, interestingly, for Type 1 diabetes markers (**Fig3b**). SV inversions and insertional mutations were identified in 4.277 out of 7.355 genes encoding for DNA strand check and elongation, platelet aggregation, and metabolism (i.e. lipid, fatty acid, glycolysis, and beta oxidation) markers (**Fig3c**). These data sustain DNA signatures relocated in physiological MN as contributors at arterial tree predisposition to atherosclerosis. Mis-segregation of all other Chr was rather dependent on oxLDL (**Fig3a**) that enhanced MNeic enrichment of all sub-classes of genes (**Suppl. Fig3b,c**), 11.269 of which were protein-coding. Interestingly, 1.235 genes were no longer enriched in pathological MN, whereas a set of 2.361 genes composed by physiological and novel protein-coding genes characterized the pathological MN. SVs were identified in almost 50% of the genes, 2.692 of which showed SV duplications (**Fig3d**) and encoded for T1D, stress induced cell senescence, inflammatory pathways (IFN, NF-kB, interleukin), oxidative damage, apoptosis, platelet aggregation, PD-1 signalling, and DNA fragmentation markers (**Fig3d**). Compared to their PN, pathological MN contained SV insertions and inversions in 2.837 genes, including those detected in physiological MN (**Fig3e**). SVs involved key markers of cell cycle checkpoint and progression, RNA transcription and translation, oxidative stress, and anti-inflammatory response (**Fig3e**). Moreover, markers of DD check and repair were mutated, including anti-atherogenic (4) Notch and Wnt signalling pathways (**Fig3e**), which comprised 1.362 out of 2.837 genes that were mutated or deleted from the PN upon oxLDL treatment (**Suppl. Fig3c,d**). In detail, SV mutations were identified in the non-homologous end joins (NHEJ) and ATM-mediated DDR of DSBs pathways (**Fig 3e** and **Suppl. Fig3c,d**), as well as in enzymes involved in innate immune system and cytosolic dsDNA sensing (**Fig3e and Suppl. Fig3c,d**). These findings indicate distinct CNVs and SVs characterizing physiological and pathological MN.

To corroborate whether selective signatures derived from asynchronous and damaged DNA, WGS was performed using Ki67 or γH2AX labelled DNA (**Suppl. Fig3e**). CNVs confirmed Chr15 and 19 high synthesis rates, increased of a 30-40% by oxLDL (**Fig3f**). OxLDL enhanced the synthesis of all Chr in MN and PN at 24h (**Fig3f**), reinforcing our hypothesis that asynchronous DNA derives from hyperproliferative ECs. In addition, Chr15 and 19 relocations in MN enhance their susceptibility to DD, which involved also selective Chr1-10 bands relocated in MN (**Fig3f**), and prominently almost all Chr relocated in PN (**Fig3f**). These data confirm the mitotic catastrophe triggered by prolonged exposure to genotoxic stresses. SV

duplications in physiological MN were confirmed for pro-inflammatory, proliferative, and ATM-dependent DDR genes (**Fig3g**), as well as SV inversions in the cadherin and Wnt signal (**Fig3h**). DNA in synthesis in pathological MN comprised genes of EC hyperproliferation and anti-apoptosis (**Fig3i**), whereas major SVs were at the charge of cell cycle check, wound repair, and metabolism (**Fig3j**), sustaining the role of oxLDL on pathological EC phenotype. Errors and DSBs affected cell cycle and genes relocated in physiological MN (**Fig3k and Suppl. Fig3f**). However, significant mutations were on charge of genes relocated in pathological MN, where genes involved in Wnt, laminin interactions, nuclear receptors, response to stress, and ATM-mediated DDR presented SV duplications and confirmed mutations (**Fig3i and Suppl. Fig3f**). These data confirmed the damage of SV containing genes in pathological MN and PN.

In parallel, we tested the transcriptional frequency of synthetized and damaged MNeic DNA. For this purpose, oxLDL treated HAoECs were co-incubated during the last hour with 5-ethynyl uridine (EU) (**Suppl. Fig3g**) to detect *de novo* RNA synthesis (17). OxLDL actively promoted the transcription of asynchronized and damaged DNA (**Fig3m**), exacerbated when EU was incubated for 24h (**Fig3m and Suppl. Fig3g**). RNA intensity normalization on heterochromatin co-localization as index of euchromatin content in active transcription confirmed that oxLDL promoted the maintenance of MNeic DNA in an euchromatin state (**Fig3m**), which positively correlated with *de novo* RNA synthesis at sites of DD (**Fig3m and Suppl. Fig3h**). Similar results were obtained by 3D confocal reconstruction of *en face* arches collected from our optimized injection and detection of EU injected in $ApoE^{-/-}$ hyperlipidaemic mice, where *de novo* RNA synthesis enhanced 5h after injection in EC and MN from arterial tree (**Fig3n**).

DDR is impaired by mutations in NHEJ and HR genes

DSBs involves activation of two pathways: the HR, activated in G_2/S and comprising RAD51 and SMC5/6 effectors, and the non-homologous end joining (NHEJ), activated throughout the cell cycle, and comprising KU80 as main effector. BRCA1 and 53BP1 mutually regulate HR and NHEJ. ATM and DNA-PKCs kinases are key upstream DDR regulators through HR and NHEJ, respectively. CNVs for DDR genes were equally identified in physiological and pathological MN and PN (**Suppl. Fig3i**) but comprised SVs mutation upon oxLDL treatment. In detail, CNVs for *TP53BP1*, *RAD51*, *XRCC5*, *SMC5/6*, *BRCA1*, and *ATM* were identified in pathological but not physiological $Ki67^{+}$MN and PN (**Suppl. Fig3j**), were SVs interested almost all genes. CNVs for *ATM* and *BRCA1* not devoted of SVs were identified in synchronized PN. Interestingly, *PRKDC* (DNA-PKCs gene) presented SV duplications in pathological MN and PN, which might reflect an inhibition of DDR (18, 19). Accordingly, except for *PRKDC* that was not detected in physiological nor pathological damaged MN, CNVs for all other DDR genes were detected (> 80%) in $\gamma H2AX^{+}$ PN (**Suppl. Fig3k**). ATM and RAD51 presented SVs already in physiological MN. In line, CVNs and PVs in MN were paralleled by lowering of DDR protein levels, especially of NHEJ-related KU80, HR-related Rad51 and slightly SMC6 markers in the nucleus of damaged ECs (**Fig4a and Suppl. Fig4a**). To analyse the levels of activated DDR effectors in MN, we developed a method to isolate proteins from FACS sorted MN and PN, which confirmed the oxLDL-mediated lowering of RAD51, and the enhancement of H2AX phosphorylation in MN and PN (**Fig4b**). Activation of ATM (**Fig4c**) and its substrate BRCA1 (**Fig4d**), but not of 53BP1 (**Suppl. Fig4b**), was lowered in ECs and damaged MN. These data sustain HR as key pathway involved in endothelial DDR, impaired upon genotoxic stresses. Accordingly, SV duplications in *PRKDC* were paralleled by a rise in DNA-PKCs activation (**Fig4e**), especially in pathological MN devoted of damaged

DNA (**Fig4e**). Chemical inhibition of DNA-PKCs by AZD7648 or LTURM34 (**Suppl. Fig4c**) confirmed that oxLDL impaired DDR by activating DNA-PKCs (**Suppl. Fig4d**).

Lamin B1 disruption affects DSBs relocation and DDR at nuclear periphery

Trimethylation of lysine 9 on H3 (H3K9me3) is a modification required to establish a heterochromatin state of damaged DNA for an efficient repair. Nuclear periphery emerged as site of heterochromatin relocation and DDR (23). Pathological ECs and MN treated 48h with oxLDL presented a reduced localization of heterochromatin (DAPI bright) compared to euchromatin (DAPI weak) foci at the periphery of main and MN membranes (**Fig5a**). Despite an increase in H3K9me3 foci was visible after early (4h) but not late exposures to oxLDL (24, 48h) (**Fig5b**), spatial co-distribution of H3K9me3 and DAPI foci indicated that oxLDL prevented DNA supercoiling, represented by a reduced and increased number of DAPI bright and weak H3K9me3^{+} foci, respectively (**Fig5c**). These data suggest that oxLDL might not impede labelling of damaged DNA, but rather affect the downstream steps leading to supercoiling of H3K9me3 marked DNA and DDR. In line, oxLDL sustained the maintenance of DNA containing DSBs (γH2AX^{+}) in an euchromatin state in both MN and PN (**Fig5d**). Independent from their H3K9me3 marks, spatial distribution analysis indicated a retention of euchromatin foci within the nucleus, far from the nuclear periphery (**Fig5c,d**). Spatial distribution of multiple stained foci indicated that oxLDL prolonged the euchromatin state of damaged DNA at the nuclear periphery (and within the nucleus) of PN, but especially of MN (**Fig5e**). Spatial co-localisation and linear intensity analysis confirmed that oxLDL did not affect the overall H3K9me3 labelling of DD, but rather the DNA supercoiling of damaged DNA (**Suppl. Fig5a**). Overall, these data sustain the transcriptional frequency promoted by oxLDL in MN, where asynchronisms might invalidate DSB check and repair at nuclear periphery.

DNA synthesis and DDR at nuclear periphery seem to be dependent on lamin B1 integrity as the main isoform characterizing MN (23). Prolonged exposure of HAoECs to oxLDL reduced the number of MN with an intact lamin B1 an enhanced the retention of MN with a disrupted lamin B1, as confirmed by IF (**Fig6a**), FACS (**Suppl. Fig5b**), and Lamin B1 protein levels within FACS sorted MN (**Fig6b**). Euchromatin comprising damaged DNA was indeed relocated at the nuclear periphery of MN showing a disrupted lamin B1 (**Fig6c**), which presented a DNA synthesis activity more elevated than intact MN (**Suppl. Fig5c**). These data corroborate the retention of DD in pathological MN and their potential transcription due to asynchronisms and related defects in DD relocation at the nuclear periphery.

Since *LMNB1* was duplicated but mutated and not expressed in pathological MN (**Suppl. Fig3i-k**), MN might depend on their PN for an efficient Lamin B1 synthesis, defective when DNA synthesis is asynchronous. This hypothesis was reinforced by FACS (**Suppl. Fig5d**) and by multiple correlation analysis of PN derivation of LMNB1^{-}γH2AX^{+}MN, which indicated DP PN as initial source (24h), and nonproliferating but damaged PN as late source (48h) of defective MN (**Fig6d**). Asynchronisms might affect the clearance of pathological MN, especially of those presenting a disrupted lamin B1 and depending on their PN for *LMNB1* expression, as indicated by oxLDL concentration-dependent longest spatial distance of pathological, but not physiological MN from their PN (**Fig6e**).

A conservatory trend was observed *in vivo*. Indeed, multiple spatial colocalization analysis of γH2AX and Ki67 foci within MN in correlation with their lamin B1 integrity on 3D *en face* aortic arched from Apoe$^{-/-}$ mice fed 4 and 12 weeks of ND or WD indicated that hyperlipidaemia impaired lamin B1 integrity in MN (**Fig6f**). High lipid levels promoted DD in defective lamin B1^{-} MN (**Fig6f**). Asynchronous DNA synthesis was enhanced initially in both

intact and disrupted MN, and later mainly in defective pathological MN containing damaged DNA (**Suppl. Fig5e**). confirming that asynchronisms sustain the retention of defective MN and the expression of relocated DNA signatures.

Nup107, Nup153, and Nup160 are components of the nuclear pore complexes (NPCs) acting as sites of DSB relocation and repair (20, 21). OxLDL did not promote CVNs nor SVs in these selective NPCs deputed to DDR (**Suppl. Fig3i-k**), as well as did not affect their location at the periphery of MN with an intact of disrupted Lamin B1 (**Suppl. Fig5f**), reinforcing the role of Lamin B1 in DD relocation and repair. To test the correlation between Lamin B1 and DDR, we performed a multiple colocalization analysis of HR markers with DD related to lamin integrity. OxLDL impaired ATM (**Fig6g**), BRCA1 (**Fig6h**), but not 53PB1 activation (**Suppl. Fig5g**) in MN with DD and a disrupted lamin B1, whereas DNA-PKCs activation was enhanced (**Fig6i**). Lack of an efficient DDR in asynchronized LMNB1^{-}MN enhanced RNA synthesis (**Fig6j**). Since transcription was promoted already at 24h in intact MN (**Suppl. Fig5c,d**), oxLDL might sustain transcription of defective transcripts or pro-atherogenic (duplicated) genes.

Altogether, our findings reveal the existence of distinct signatures and SVs selectively characterizing physiological and pathological ECs lining arterial tree. Like cancer cells, our work exposes a targetable vulnerability for proliferating ECs that display MN, as pivotal recipients of pro-atherogenic genes that efficiently duplicate synchronously to their principal nucleus. This was confirmed by detection of distinct locus in MN associated with cardiovascular disease incidences (18) across live cell imaging and sequencing in mouse and human cell lines, *in vivo* and *in vitro*. Our work also indicates that asynchronisms between MN and PN promoted by oxLDL and hyperlipidaemia determine defective DDR and MN retention by affecting key anti-atherogenic genes relocated in MN, including the cell cycle check and HR. As lamin B1 play pivotal roles in DSB repair by interacting with HR enzymes (i.e. BRCA1 and RAD51) at the nuclear periphery (21), mutations in LMNB1 by hyperlipidaemia enhances EC vulnerability to DD-enriched MN retention. Our findings furthermore suggest a potential transcriptional activity of distinct locus associated with cardiovascular diseases, as well as of additional pro-angiogenic genes deriving from pathological MN, reinforcing the contribution of key SVs in the onset and progression of atherosclerosis. As DDR efficiency, especially by ATM, leads to hyperlipidaemia and atherosclerosis progression, the recent findings indicating that acceleration of DDR by statin-mediated ATM phosphorylation attenuates DD (22) reinforce the contribution of therapies directed against pathological MN to treat atherosclerosis.

References

1. Hong YM. Atherosclerotic cardiovascular disease beginning in childhood. Korean circulation journal. 2010;40(1):1-9.
2. Allam AH, Thompson RC, Wann LS, Miyamoto MI, Nur El-Din Ael H, El-Maksoud GA, et al. Atherosclerosis in ancient Egyptian mummies: the Horus study. JACC Cardiovascular imaging. 2011;4(4):315-27.
3. VanderLaan PA, Reardon CA, Getz GS. Site Specificity of Atherosclerosis. Arteriosclerosis, Thrombosis, and Vascular Biology. 2004;24(1):12-22.
4. Natarelli L, Schober A. MicroRNAs and the response to injury in atherosclerosis. Hamostaseologie. 2015;35(2):142-50.
5. Libby P. The changing landscape of atherosclerosis. Nature. 2021;592(7855):524-33.
6. Crasta K, Ganem NJ, Dagher R, Lantermann AB, Ivanova EV, Pan Y, et al. DNA breaks and chromosome pulverization from errors in mitosis. Nature. 2012;482(7383):53-8.
7. Natarelli L, Geißler C, Csaba G, Wei Y, Zhu M, di Francesco A, et al. miR-103 promotes endothelial maladaptation by targeting lncWDR59. Nat Commun. 2018;9(1):2645.
8. Uryga A, Gray K, Bennett M. DNA Damage and Repair in Vascular Disease. Annual Review of Physiology. 2016;78(1):45-66.
9. Shimizu N. Molecular mechanisms of the origin of micronuclei from extrachromosomal elements. Mutagenesis. 2011;26(1):119-23.
10. Zhang CZ, Spektor A, Cornils H, Francis JM, Jackson EK, Liu S, et al. Chromothripsis from DNA damage in micronuclei. Nature. 2015;522(7555):179-84.
11. HEINLOTH A, HEERMEIER K, RAFF U, WANNER C, GALLE J. Stimulation of NADPH Oxidase by Oxidized Low-Density Lipoprotein Induces Proliferation of Human Vascular Endothelial Cells. Journal of the American Society of Nephrology. 2000;11(10):1819-25.
12. Liu H, Zhang H, Wu X, Ma D, Wu J, Wang L, et al. Nuclear cGAS suppresses DNA repair and promotes tumorigenesis. Nature. 2018;563(7729):131-6.
13. Mackenzie KJ, Carroll P, Martin CA, Murina O, Fluteau A, Simpson DJ, et al. cGAS surveillance of micronuclei links genome instability to innate immunity. Nature. 2017;548(7668):461-5.
14. Schober A, Nazari-Jahantigh M, Wei Y, Bidzhekov K, Gremse F, Grommes J, et al. MicroRNA-126-5p promotes endothelial proliferation and limits atherosclerosis by suppressing Dlk1. Nature medicine. 2014;20(4):368-76.
15. Uxa S, Castillo-Binder P, Kohler R, Stangner K, Müller GA, Engeland K. Ki-67 gene expression. Cell Death & Differentiation. 2021;28(12):3357-70.
16. Lusis AJ. Genetics of atherosclerosis. Trends in genetics : TIG. 2012;28(6):267-75.
17. Palozola KC, Donahue G, Liu H, Grant GR, Becker JS, Cote A, et al. Mitotic transcription and waves of gene reactivation during mitotic exit. Science. 2017;358(6359):119-22.
18. Yue X, Bai C, Xie D, Ma T, Zhou P-K. DNA-PKcs: A Multi-Faceted Player in DNA Damage Response. Frontiers in Genetics. 2020;11.
19. Maréchal A, Zou L. DNA damage sensing by the ATM and ATR kinases. Cold Spring Harb Perspect Biol. 2013;5(9):a012716.
20. Lamm N, Rogers S, Cesare AJ. Chromatin mobility and relocation in DNA repair. Trends in Cell Biology. 2021;31(10):843-55.
21. Kramarz K, Schirmeisen K, Boucherit V, Ait Saada A, Lovo C, Palancade B, et al. The nuclear pore primes recombination-dependent DNA synthesis at arrested forks by promoting SUMO removal. Nature Communications. 2020;11(1):5643.
22. Mahmoudi M, Gorenne I, Mercer J, Figg N, Littlewood T, Bennett M. Statins use a novel Nijmegen breakage syndrome-1-dependent pathway to accelerate DNA repair in vascular smooth muscle cells. Circulation research. 2008;103(7):717-25.
23. Hartmann P, Zhou Z, Natarelli L, Wei Y, Nazari-Jahantigh M, Zhu M, et al. Endothelial Dicer promotes atherosclerosis and vascular inflammation by miRNA-103-mediated suppression of KLF4. Nat Commun. 2016;7:10521.
24. Rausch T, Zichner T, Schlattl A, Stütz AM, Benes V, Korbel JO. DELLY: structural variant discovery by integrated paired-end and split-read analysis. Bioinformatics. 2012;28(18):i333-i9.

25. Chen EY, Tan CM, Kou Y, Duan Q, Wang Z, Meirelles GV, et al. Enrichr: interactive and collaborative HTML5 gene list enrichment analysis tool. BMC bioinformatics. 2013;14:128.
26. Kuleshov MV, Jones MR, Rouillard AD, Fernandez NF, Duan Q, Wang Z, et al. Enrichr: a comprehensive gene set enrichment analysis web server 2016 update. Nucleic acids research. 2016;44(W1):W90-7.
27. Xie Z, Bailey A, Kuleshov MV, Clarke DJB, Evangelista JE, Jenkins SL, et al. Gene Set Knowledge Discovery with Enrichr. Current Protocols. 2021;1(3):e90.

Acknowledgments
We thank Dr. Michael Hirstov for assistance with FACS sorter; Dr. Peter Liu at the BGI Genomics for help with optimization of library preparation and WGS. This work was supported by Deutsche Forschungsgemeinschaft (DFG), TRR267, and SFB1123 to C.W. and L.N.

Author contribution
L.N. and C.W. designed the study and wrote the manuscript. L.N. carried out all experiments *in vivo* and *in vitro* and analysed the data. Z.A.K. and E.M.F. helped in performing western blots. L.P. analysed the WGS data. Z.A.K. helped with cell culture. E.M.F. helped with the immunofluorescence analysis and FACS sorting. T.M. contributed to the WGS analysis. All authors discussed the results and commented on the manuscript.

Competing Financial Interests
The authors declare no competing financial interests.

Online content, data and materials availability
Materials and Methods including experimental details and reagents can be found in the Supplementary Materials. All data associated with this study are present in the main text or the Supplementary Materials. RNAseq data sets are available upon request.

Fig1. Shear stress-, oxLDL-, and hyperlipidemia-mediated MN formation in ECs.
(a) HAoECs were cultured under LSS (5 dyne cm^{-2}) or HSS (10 dyne cm^{-2}) and incubated with 5-ethynyl-2´-deoxyuridine (EdU) to evaluate the percentage of proliferating ECs containing MN. Data are expressed as percentage of total ECs (n= 6-9 samples per group). **(b)** HAoECs were let grown for 4, 24, and 48h and stained for immunofluorescence detection and quantification of $Ki67^+$ ECs, and to analyse MN content. Data are normalized on total ECs. **(c,d)** $ApoE^{-/-}$ mice fed 4 and 12 weeks of normal diet (ND). Arches and thoracic aortae were prepared *en face* and stained with Ki67 and CD31 EC marker. Nuclei were stained with DAPI. 3D images were collected using a Confocal microscope. Picture is aortic arch *en face*, indicating $CD31^+$ cells, which are $Ki67^+$ and show MN. (n= 5 mice per group). **(e)** HAoECs were synchronized or not and treated for 6 hours with 200 ng/ml Nocodazole to synchronise them in metaphase to analyse the cell cycle phase at which chromosome mis-segregation and MN formation occurred. HAoECs were transfected with the BacMam vectors containing the GFP-geminin gene and the RFP-Cdt1 gene and live recorded a climate chamber STED microscope. Time of picture acquisition is indicated in minutes. Arrowheads indicate micronuclei (MN) and principal nuclei (PN) DNA division. Images are representatives of 3 independent experiments. Scale bar: 10µm. **(f,h)** HAoECs were treated with 25, 50, or 100 µg/ml oxLDL for 4, 24, and 48h to analyse the number of MN in proliferating and non-proliferating ECs. **(h)** HAoECs were treated with oxLDL and synchronized as in **(e)** to analyse the cell cycle phase and quantify the bridges in cytokinesis or transfected with BacMam vectors to quantify the asynchronous DNA synthesis. Mis-segregation in interphase was quantified by dividing the n. of EC with mis-segregation in metaphase counted in oxLDL on those counted in control (%) (n= 10 per group). Images are representatives of 3 independent experiments. Scale bar: 10µm. (**g,i,j**) Aortic arches of $ApoE^{-/-}$ fed 4 and 12 weeks of normal or high fat diet (ND, HFD) were *en face* stained with Ki67 to analyse the effect of HFD on **(g)** EC proliferation, MN formation, **(i)** in proliferative and non-proliferative ECs, and **(j)** to analyse the number of asynchronized MN and PN ($Ki67\ MN^+PN^-$ and MN^-PN^+). The number of MN^+PN^+ was used as marker of synchronism. CD31 was used as EC marker. Nuclei were stained with DAPI (n = 4-6 mice per group). Scale bar: 5 µm. *p<0.05; **p<0.01; ***p<0.001.

Fig2. Effect of oxLDL and hyperlipidaemia on DD in proliferative and non-proliferative ECs. HAoECs were treated with 50 µg/ml oxLDL for 4, 24, and 48h to analyse the number of γH2AX^{+} Ki67^{-} and γH2AX^{+}Ki67^{+} double positive (DP) **(a)** ECs and **(b)** MN (n= 5-7 per group). Moreover, it was analysed the number of MN **(c)** containing damaged DNA (γH2AX^{+} MN, which can include also the Ki67^{+} MN) deriving from all γH2AX^{+} ECs (which include also the Ki67^{+} ECs), from γH2AX^{+} Ki67^{-} PN, from **(d)** DP and from γH2AX^{+} Ki67^{-} ECs, plus the DP MN deriving from DP ECs (n= 5-7 per group). **(e,f)** Aortic arches of ApoE$^{-/-}$ fed 4 and 12 weeks of normal or high fat diet (ND, HFD) were *en face* stained for Ki67 and γH2AX to analyse the effect on **(e)** DNA damage and proliferation, and MN. **(f)** The number of DD enriched MN (γH2AX^{+} Ki67^{-} MN) deriving from γH2AX^{+} Ki67^{-} ECs and the number of DP MN deriving from DP ECs was analysed as well. CD31 was used as EC marker. **(g)** HAoECs treated or not 48h with oxLDL were incubated till 6h with ctrl or oxLDL MN to analyse their retention, and activation of reactive markers. Nuclei were stained with DAPI (n = 5 mice per group). Scale bar: 5 µm. *p<0.05; **p<0.01; ***p<0.001.

Figure 3. Whole Genome Sequencing and gene pathways enrichment analysis of MN and PN genes. (a) Aneuploidy from WGS of MN and PN from HAoECs treated or not with oxLDL for 24h deriving from the analysis of CNVs. (**b-e**) Analysis and comparison of enriched and mutated genes has been done between: MN vs. PN from untreated (group A) or oxLDL treated (group B) HAoECs, MN vs. MN and PN vs. PN from untreated vs. oxLDL treated ECs (group C and D, respectively). Enrichment of genes (gain genes) and genomic classification from oxLDL treated HAoECs have been represented in the histogram graph. **(f)** CNVs in proliferative MN and PN (Ki67, 24h) or damaged (γH2AX, 48h) and **(g-l)** enrichment of mutated genes. Scatter plots represents the most significant pathways. Odds ratio colour and bubble graphs represent the number of genes within the same pathway. Genes are graphed according to their odds ratio and the logarithmic negative p value. The pathways identified within all Enrichr databases are in bold. (m) EU staining and quantification in MN containing damaged DNA after 1h or 24h of EU incubation following oxLDL treatment, or (n) in ApoE-/- mice fed 12 weeks of HFD. Euchromatin correlation with RNA synthesis (n= 4 per group, or mice). Scale bar: 10 µm. *p<0.05; **p<0.01; ***p<0.001.

Fig4. Effect of oxLDL and hyperlipidaemia on DDR systems. HAoECs were treated or not with 50µg/ml oxLDL for the time indicated to analyse the **(a,c-e)** total, **(b)** nuclear, **(c-e)** and MN levels of key parkers of DDR involved in HR (P-ATM, BRCA1, Rad51) or NHEJ (Ku80, DNA-PKCs), including in MN containing damaged DNA (n=4 per group). Scale bar: 5 µm. *p<0.05; **p<0.01; ***p<0.001.

Figure 5. OxLDL supercoiling of damaged DNA at nuclear periphery. HAoECs were treated or not with 50µg/ml oxLDL for the time indicated to analyse the number of heterochromatin (DAPI bright) or euchromatin (DAPI weak) foci **(a)** in principal nuclei (PN) or MN, **(b,c)** co-localizing with the heterochromatin marker H3K9me3, and (d,e) containing damaged DNA (γH2AX). **(a)** Red arrowhead: foci far from nuclear periphery; blue arrowhead: DAPI bright at nuclear periphery. **(b)** Yellow arrowhead: foci far from nuclear periphery; blue arrowhead: DAPI bright at nuclear periphery. **(c)** Yellow arrowhead: euchromatin foci; blue arrowhead: heterochromatin foci. Scale bar: 5 µm. *p<0.05; **p<0.01; ***p<0.001.

Fig6. Effect of oxLDL and hyperlipidaemia on MN lamina assembly and DDR. (a-e) HAoECs were treated with 50µg/ml oxLDL for 4, 24, and 48h for immunofluorescence analysis of **(a,b)** Lamin B1 in MN and PN, related to **(c)** MN γH2AX levels. MN were analysed according to their Lamin B1 integrity as MN with an intact (Lamin $B1^+$ MN) or disrupted lamina (Lamin $B1^-$MN). Moreover, **(d)** it was analysed the percentage of MN with DNA damage and a disrupted lamina (Lamin $B1^-$ $\gamma H2AX^+$ MN) deriving from ECs with DNA damage ($\gamma H2AX^+$ MN, $\gamma H2AX^+$ $Ki67^-$ PN) or with an active DNA synthesis (DP, $\gamma H2AX^+$ $Ki67^+$ PN) (n= 5 per group). **(e)** The distance between EC nuclei and their respective MN, and the distance between EC nuclei and MN with a disrupted lamin B1 was analysed in HAoECs treated with 50 or 100 µg/ml oxLDL for 48h using the Leica integrated algorithm (n= 50 MN per group). **(f)** Aortic arches of $ApoE^{-/-}$ fed 4 and 12 weeks of normal or high fat diet (ND, HFD) were *en face* stained for Ki67, γH2AX, and Lamin B1 to analyse the effect of HFD on DNA damage on MN Lamin B1 disruption (Lamin $B1^+$ or Lamin $B1^-$ $CD31^+$ ECs), and containing duplicating damaged DNA ($\gamma H2AX^+$ MN) **(g-i)** OxLDL treated HAoECs were stained with anti-Lamin B1, $\gamma H2AX^+$, alone or in combination with **(g)** P-ATM, **(h)** BRCA1, **(i)** DNA-PKCe antibodies to analyse the effect of oxLDL on protein localization in MN according to lamin B1 integrity and DNA damage in MN (n= 5 per group). **(j)** HAoECs were treated with 50µg/ml oxLDL for 24 and 48h, and 5-ethynyl uridine (EU) for 1h to detect newly synthetized RNA and RNA levels in MN stained with Lamin B1 and γH2AX. DAPI was used to stain nuclei and MN (n= 6 per group). Scale bar: 5 µm. *p<0.05; **p<0.01; ***p<0.001.

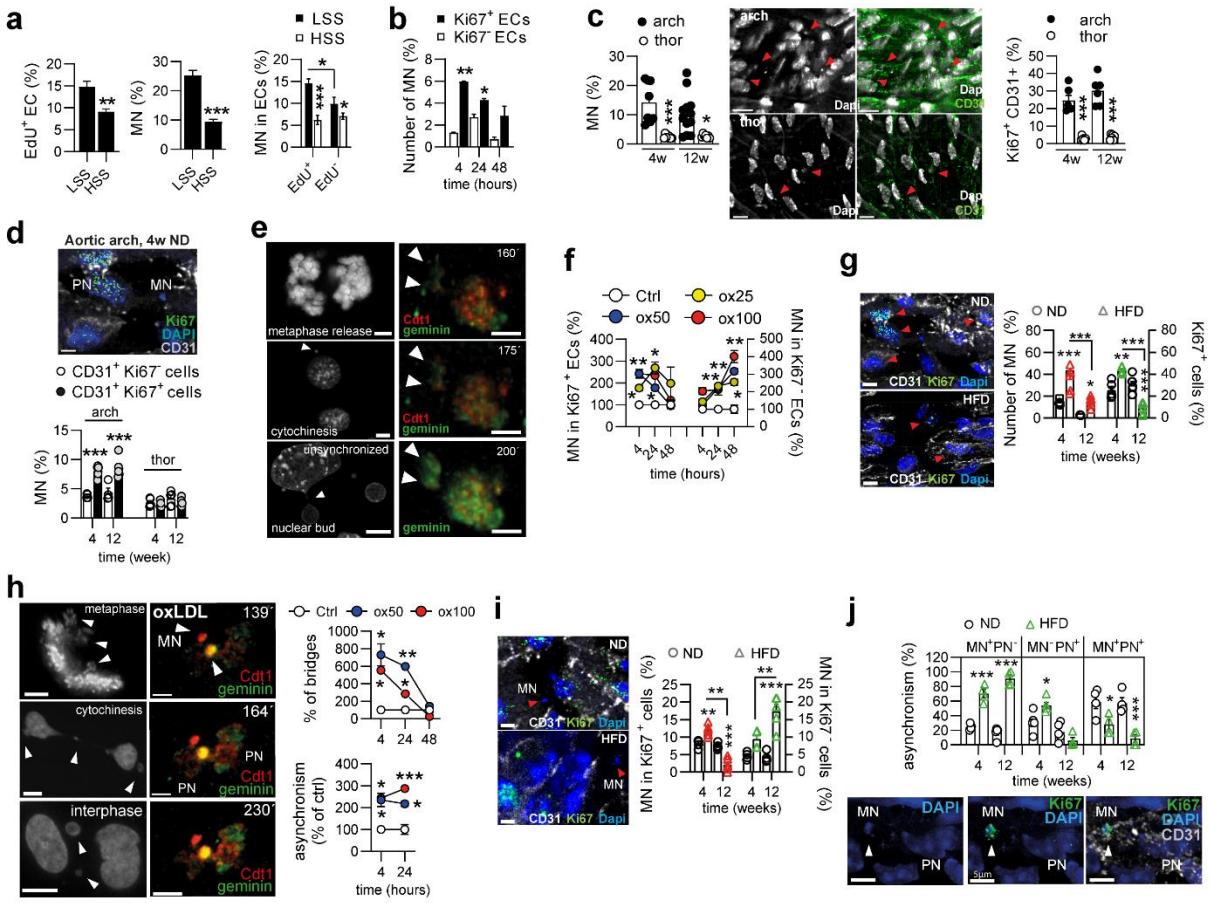
a
b
c
d
e
f
g
h
i
j
LSS
HSS
Ki67+ ECs
Ki67- ECs
arch
thor
4w
12w
Aortic arch, 4w ND
PN
MN
Ki67
DAPI
CD31
CD31+ Ki67- cells
CD31+ Ki67+ cells
time (week)
time (hours)
metaphase release
cytochinesis
unsynchronized
nuclear bud
Cdt1
geminin
Ctrl
ox25
ox50
ox100
MN in Ki67+ ECs (%)
MN in Ki67- ECs (%)
ND
HFD
Number of MN (%)
Ki67+ cells (%)
time (weeks)
oxLDL
metaphase
cytochinesis
interphase
% of bridges
asynchronism (% of ctrl)
MN in Ki67+ cells (%)
MN in Ki67- cells (%)
asynchronism (%)
MN+PN-
MN-PN+
MN+PN+
Sum

Figure 1

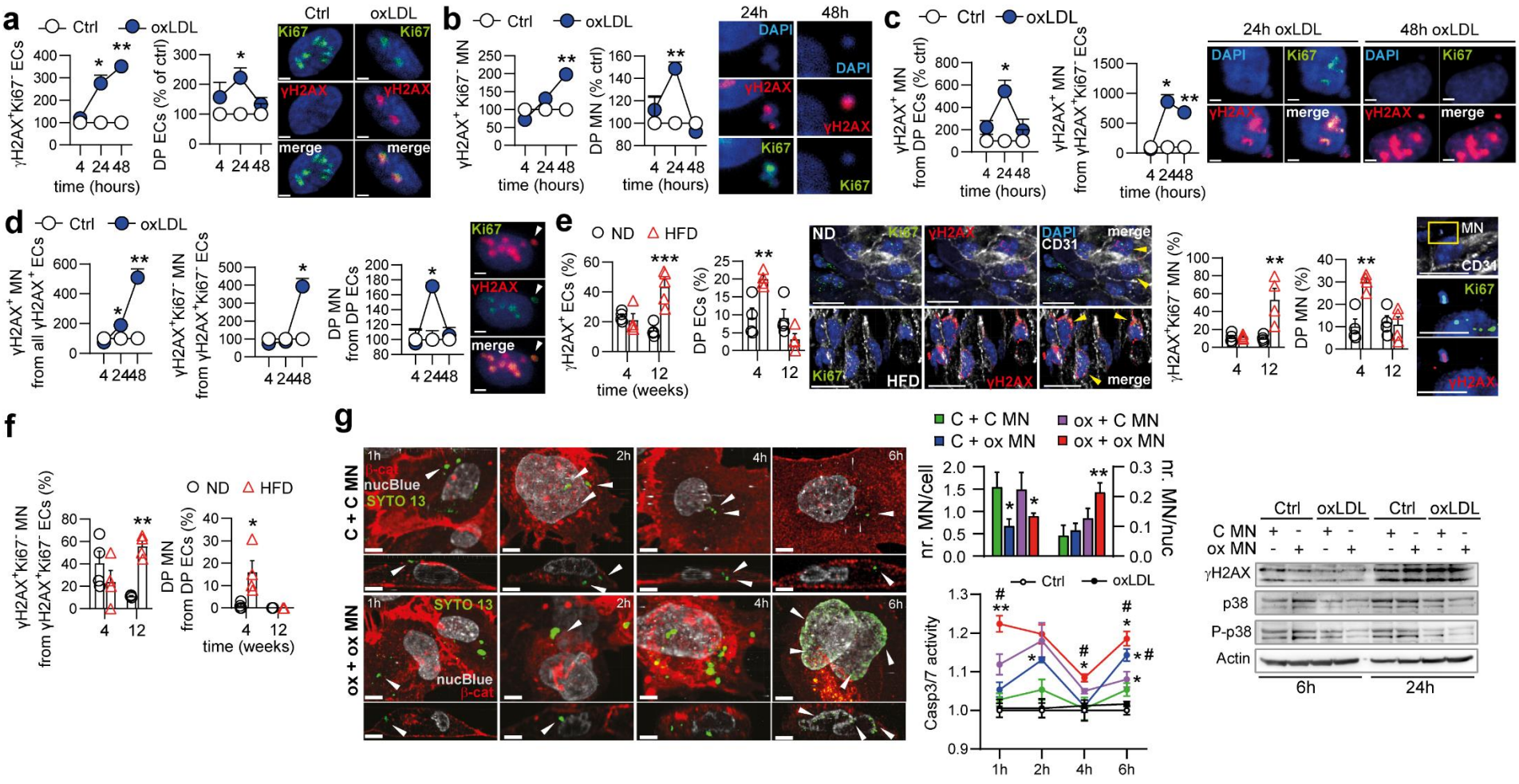
a
Ctrl
oxLDL
γH2AX+Ki67- ECs
DP ECs (% of ctrl)
time (hours)
Ki67
γH2AX
merge
b
γH2AX+ Ki67- MN
DP MN (% ctrl)
24h
48h
DAPI
c
γH2AX+ MN from DP ECs (% ctrl)
γH2AX+ MN from γH2AX+Ki67- ECs
24h oxLDL
48h oxLDL
d
γH2AX+ MN from all γH2AX+ ECs
γH2AX+Ki67- MN from γH2AX+Ki67- ECs
DP MN from DP ECs
e
ND
HFD
γH2AX+ ECs (%)
DP ECs (%)
time (weeks)
CD31
MN
γH2AX+Ki67- MN (%)
DP MN (%)
f
γH2AX+Ki67- MN from γH2AX+Ki67- ECs (%)
DP MN from DP ECs (%)
g
C + C MN
ox + ox MN
β-cat
nucBlue
SYTO 13
C + C MN
ox + C MN
C + ox MN
ox + ox MN
nr. MN/cell
nr. MN/nuc
Casp3/7 activity
C MN
ox MN
γH2AX
p38
P-p38
Actin
6h
24h

Figure 2

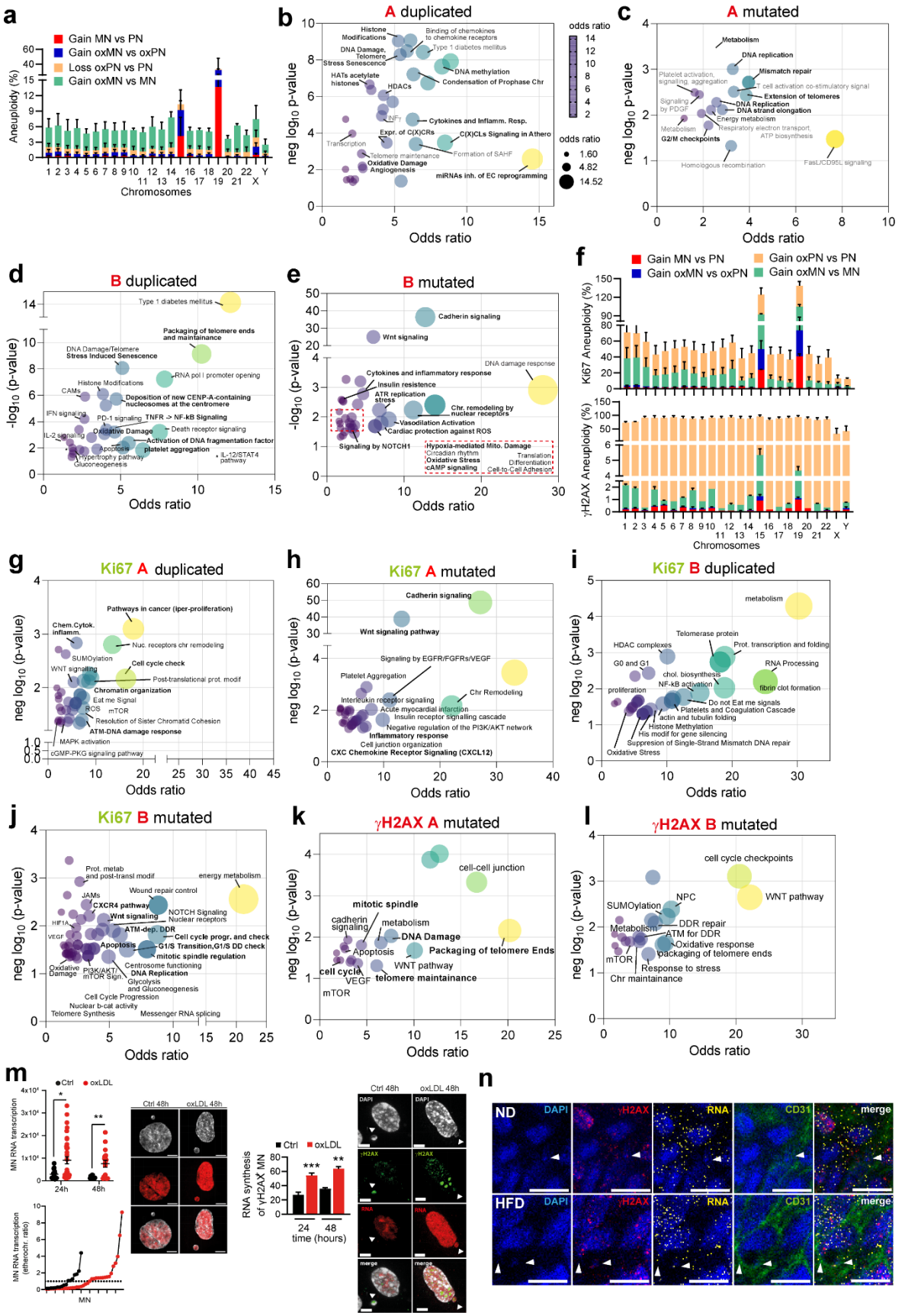
a
Gain MN vs PN
Gain oxMN vs oxPN
Loss oxPN vs PN
Gain oxMN vs MN
Aneuploidy (%)
Chromosomes
b
A duplicated
neg log10 p-value
Odds ratio
odds ratio
c
A mutated
d
B duplicated
-log10 (p-value)
e
B mutated
f
Gain MN vs PN
Gain oxPN vs PN
Gain oxMN vs oxPN
Gain oxMN vs MN
Ki67 Aneuploidy (%)
γH2AX Aneuploidy (%)
g
Ki67 A duplicated
h
Ki67 A mutated
i
Ki67 B duplicated
j
Ki67 B mutated
k
γH2AX A mutated
l
γH2AX B mutated
m
Ctrl
oxLDL
MN RNA transcription
RNA synthesis of γH2AX MN
time (hours)
n
ND
HFD
DAPI
γH2AX
RNA
CD31
merge

Figure 3

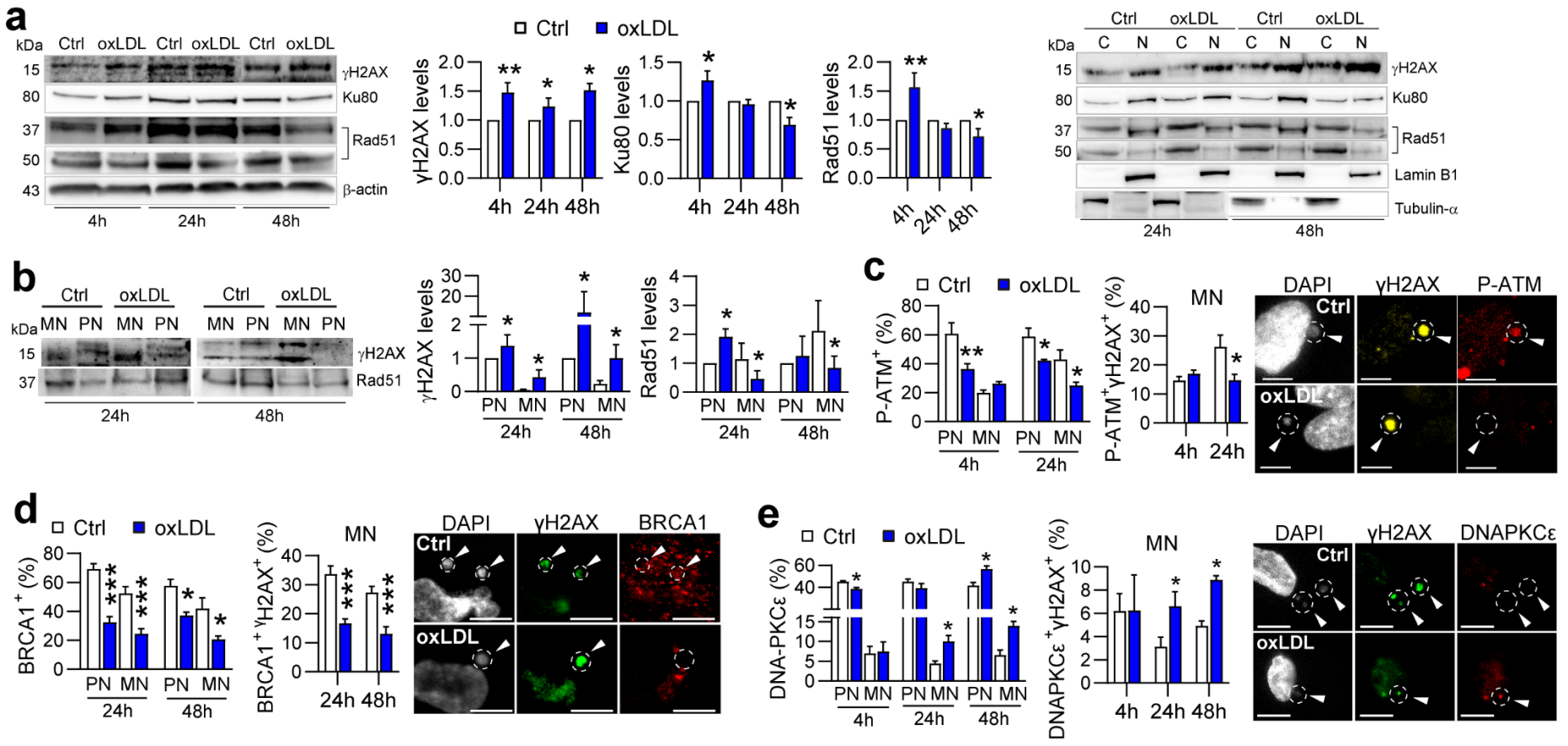
a
kDa
Ctrl
oxLDL
15
80
37
50
43
γH2AX
Ku80
Rad51
β-actin
4h
24h
48h
γH2AX levels
Ku80 levels
Rad51 levels
C
N
Lamin B1
Tubulin-α
b
MN
PN
c
P-ATM+ (%)
P-ATM+γH2AX+ (%)
DAPI
P-ATM
d
BRCA1+ (%)
BRCA1+γH2AX+ (%)
BRCA1
e
DNA-PKCε (%)
DNAPKCε+γH2AX+ (%)
DNAPKCε

Figure 4

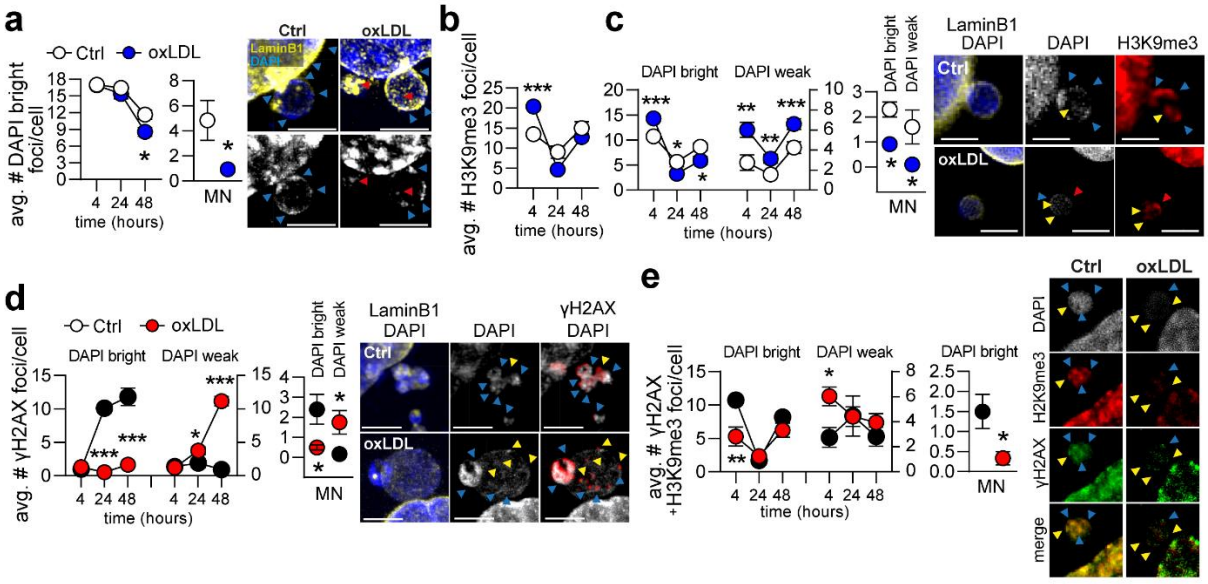
a
Ctrl
oxLDL
avg. # DAPI bright foci/cell
time (hours)
MN
LaminB1
DAPI
b
avg. # H3K9me3 foci/cell
time (hours)
c
DAPI bright
DAPI weak
time (hours)
MN
LaminB1
DAPI
DAPI
H3K9me3
d
avg. # γH2AX foci/cell
DAPI bright
DAPI weak
time (hours)
MN
LaminB1
DAPI
DAPI
γH2AX
DAPI
e
avg. # γH2AX +H3K9me3 foci/cell
DAPI bright
DAPI weak
time (hours)
MN
DAPI
H2K9me3
γH2AX
merge

Figure 5

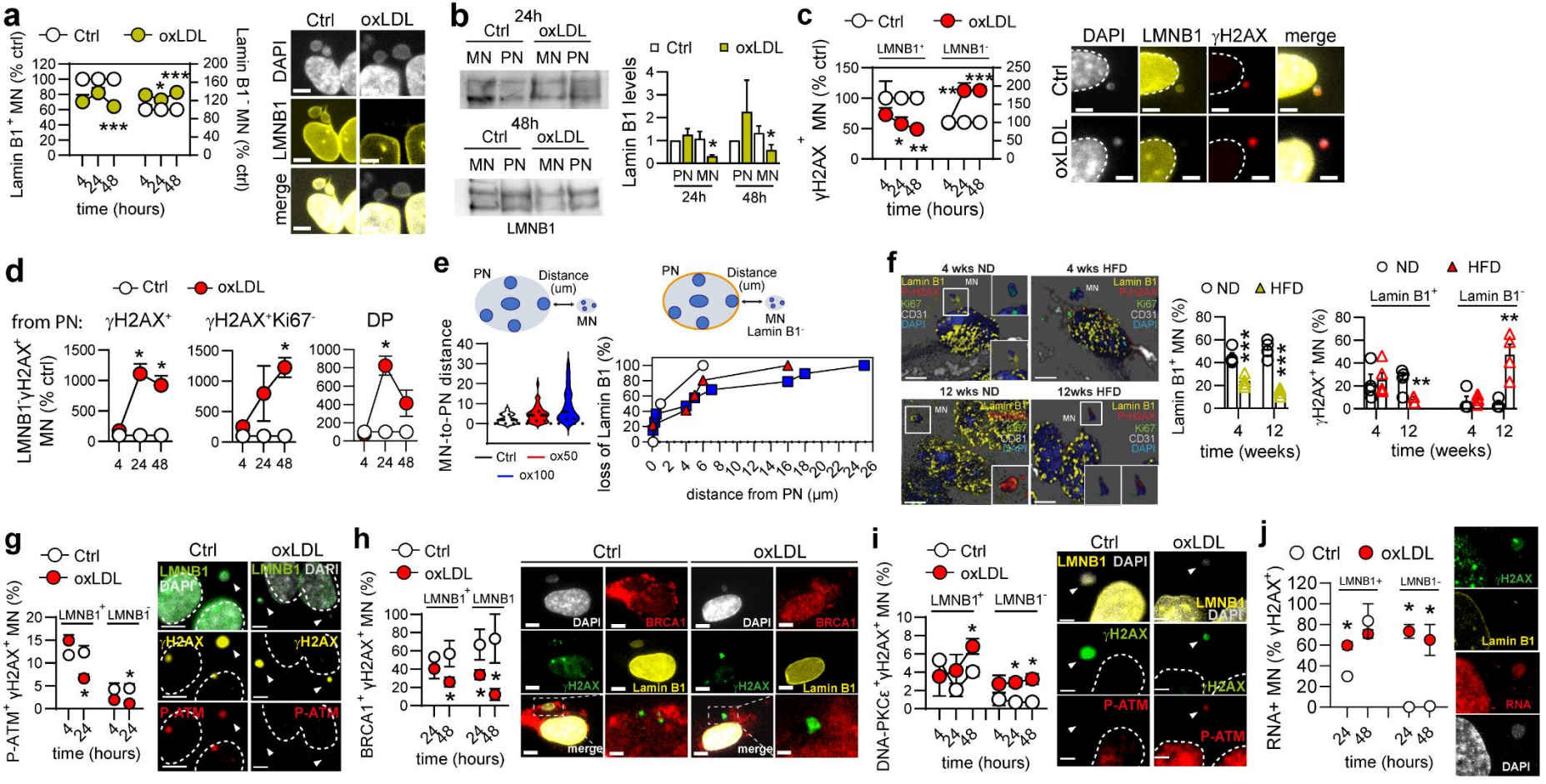
a
Ctrl
oxLDL
Lamin B1+ MN (% ctrl)
Lamin B1- MN (% ctrl)
time (hours)
DAPI
LMNB1
merge
b
24h
48h
MN PN MN PN
LMNB1
Lamin B1 levels
PN MN
c
LMNB1+
LMNB1-
γH2AX+ MN (% ctrl)
DAPI LMNB1 γH2AX merge
d
from PN: γH2AX+ γH2AX+Ki67- DP
LMNB1-γH2AX+ MN (% ctrl)
e
PN
Distance (um)
MN
MN-to-PN distance
ox50
ox100
loss of Lamin B1 (%)
Lamin B1-
distance from PN (μm)
f
4 wks ND
4 wks HFD
12 wks ND
12wks HFD
ND
HFD
Lamin B1+ MN (%)
γH2AX+ MN (%)
time (weeks)
g
P-ATM+ γH2AX+ MN (%)
h
BRCA1+ γH2AX+ MN (%)
i
DNA-PKcs+ γH2AX+ MN (%)
j
RNA+ MN (% γH2AX+)

Figure 6